Article

Improved Methanol-to-Formate Electrocatalytic Reaction by Engineering of Nickel Hydroxide and Iron Oxyhydroxide Heterostructures

Ning Jian [1,2], Huan Ge [1,2], Yi Ma [1,2], Yong Zhang [1,2], Luming Li [1,2], Junfeng Liu [3], Jing Yu [4], Canhuang Li [4], and Junshan Li [1,2,*]

[1] School of Mechanic Engineering, Chengdu University, Chengdu 610106, China
[2] Institute for Advanced Study, Chengdu University, Chengdu 610106, China
[3] Institute for Energy Research, Jiangsu University, Jiangsu 212013, China
[4] Catalonia Institute for Energy Research-IREC, Sant Adrià de Besòs, Barcelona 08930, Spain
* Correspondence: lijunshan@cdu.edu.cn
Received: 8 March 2025; Revised: 21 March 2025; Accepted: 25 March 2025; Published: 27 March 2025

Abstract: Electrocatalytic methanol oxidation reaction (MOR) holds significant value in the chemical industry, as it enables the treatment of methanol-containing wastewater and promotes hydrogen production from water. This study investigates a strategy based on tuning-composition of metal elements to optimize MOR performance, aiming to outperform the current cost-effective and efficient catalysts. To this end, nickel hydroxide and iron oxyhydroxide heterostructures were synthesized through a facile hydrothermal routine, and the catalytic performance of three different Ni/Fe ratios in MOR was examined in alkaline media. Among them, the material with equal Ni/Fe ratio exhibited the best catalytic activity, maintaining a high current density of ~66 mA cm^{-2} at 1.5 V vs. RHE in 1 M KOH electrolyte with 1 M methanol. Moreover, this developed electrode showed a Faradaic efficiency (FE) of 98.5% for formate production within a continuous 12 h test. Furthermore, density function theory (DFT) calculation was applied to unravel the methanol-to-formate conversion mechanism that was enhanced by the proper Ni/Fe ratio. These results demonstrate the high efficiency and selectivity of efficient methanol-to-formate conversion on NiFe-based materials, providing a promising a non-precious catalyst for electrocatalytic upgrading methanol to value-added formate.

Keywords: electrocatalysis; methanol oxidation reaction; formate production; hydrogen evolution reaction; electrocatalytic upgrading

1. Introduction

The transition to a carbon-neutral society calls for the effective integration of renewable energy sources like solar, hydro, and wind, which require reliable storage solutions due to fluctuating characteristics [1]. Thus, efficient energy storage is highly demanded. Among the electrochemical methods, in particular the water splitting into hydrogen and oxygen, are promising due to their scalability, efficiency, and simplicity [2–5]. As a half reaction, oxygen evolution reaction (OER) at the anode, is the key step due to its sluggish kinetics, largely reducing the efficiency of electrocatalytic water splitting [6–8]. To address this drawback, the OER can be replaced with the low-potential electrooxidation of small organic molecules, enhancing HER efficiency while simultaneously converting these organic compounds into value-added chemicals [9–14]. This strategy presents a more economical strategy for energy storage and conversion.

Among the common organics, methanol is a particularly attractive candidate due to its cost-effectiveness, ease of transport, practicality, and widespread availability [15]. Additionally, the anodic methanol oxidation reaction (MOR) offers a selective and economically favorable pathway for the production of formate, an important industrial intermediate [11]. Furthermore, the anodic MOR operates at a considerably lower potential than the OER, enabling an efficient HER with moderate energy requirements [16]. Additionally, MOR can produce formic acid (or existing in the form of formate in alkaline media) with high selectivity [17–19]. Nevertheless, for this approach to be economically viable, it is essential to develop cost-effective, high-performance MOR electrocatalysts.

Previous reports show platinum-based catalysts excel in MOR efficiency and the potential usage for fuel cells [20–23]. However, to compete with fossil fuels, the hydrogen production from water requires cost-effective and stable and cheap electrode materials, particularly nickel-based catalysts due to the formation of NiOOH, a key intermediate in the reaction in alkaline media [24–28]. To further improve the MOR performance, nickel catalysts, often enhanced with other metal elements, are especially promising for MOR [11,29–32]. Expanding on this, nickel-iron based materials specially offer an exceptional option for methanol-to-formate conversion, with a focus on optimizing Ni/Fe ratios for enhanced performance [33].

Here in this work, we have developed a novel catalyst based on nickel hydroxide and iron oxyhydroxide, synthesized via hydrothermal methods. By varying the Ni and Fe ratios, we aimed to identify the optimal Ni/Fe composition for MOR, achieving a cost-effective and efficient approach to formic acid production. Experimental evidence further suggests that combining Ni with Fe enhances the catalytic MOR performance. To figure out the composition and structure influence on the methanol-to-formate performance, first-principle-based density functional theory (DFT) calculations were also performed.

2. Experimental Section

2.1. Chemicals and Reagents

All chemicals and reagents, including nickel chloride hexahydrate ($NiCl_2·6H_2O$, 98%, Sigma-Aldrich, Shanghai, China), iron(III) chloride tetrahydrate ($FeCl_2·4H_2O$, 98%, Sigma-Aldrich, Shanghai, China), urea (CH_4N_2O, 99%, Greagent, Shanghai, China), ammonium fluoride (NH_4F, 97%, Greagent, Shanghai, China) anhydrous methanol (MeOH, 99.8%, Sigma-Aldrich, Shanghai, China), potassium hydroxide (KOH, 85%, Sigma-Aldrich, Shanghai, China), Nafion solution (10 wt.% perfluorinated ion-exchange resin in water, Shanghai, China), potassium carbonate (K_2CO_3, 99.99%, Adamas, Shanghai, China), and carbon black (CB, Vulcan XC72, Shanghai, China), were used directly without additional purification. These included High-purity water with a resistivity of 18.2 MΩ cm was prepared using a home-made system.

2.2. Materials Synthesis

In a typical synthesis, 119 mg of $NiCl_2·6H_2O$, 22 mg of $FeCl_2·4H_2O$, 600 mg of urea, and 110 mg of NH_4F were dissolved in 60 mL of deionized water in a beaker. The resulting solution was transferred to an autoclave and maintained at 120 °C for 15 h. After naturally cooling to room temperature, the obtained product was rinsed twice with water and ethanol, then dried at 60 °C for 10 h. To tune the Ni/Fe atomic ratio in the electrocatalyst, the initial molar ratio of $NiCl_2·6H_2O$ to $FeCl_2·4H_2O$ were adjusted to 1:3 and 1:1, with the remaining synthesis process kept unchanged.

2.3. Materials Characterization

The crystal structure of the as-synthesized sample was analyzed using X-ray diffraction (XRD) with a Bruker AXS D8 (Karlsruhe, Germany) Advance instrument (Cu Kα radiation, λ = 1.5106 Å). Scanning electron microscopy (SEM) was conducted on a Zeiss GeminiSEM microscope (Oberkochen, Germany), which was equipped with an energy dispersive spectroscopy (EDS) analyzer for elemental analysis. High-resolution transmission electron microscopy (HRTEM) and scanning transmission electron microscopy (STEM) were performed using a Tecnai F20 microscope (Eindhoven, Netherlands). The high-angle annular dark-field (HAADF) STEM imaging mode was combined with electron energy loss spectroscopy (EELS) using a Gatan Quantum filter on the same microscope. Additionally, X-ray photoelectron spectroscopy (XPS) measurements were carried out on a SPECS system. The X-ray absorption fine structure (XAFS) technique was employed to analyze the electronic properties and local chemical environment of Ni species in the samples. Prior to measurements, the samples were uniformly coated onto 3 M tape. Ni K-edge XAFS spectra were collected in the energy range of 8230–9030 eV. To ensure accuracy, the spectra of all samples were calibrated using a standard Ni foil, with data collected in transmission mode. The XAFS data were processed using the Demeter 0.9.26 software package (Athena and Artemis).

2.4. Electrochemical Characterization

The electrochemical properties were evaluated using a CorrTest CS2350H workstation (Wuhan, China) under standard conditions. A three-electrode setup was utilized, consisting of a platinum wire as the counter electrode (CE), a glassy carbon (GC) electrode (0.196 cm^2) as the working electrode (WE), and an Hg/HgO electrode as the

reference electrode (RE). For the preparation of the WE, 10 mg of dried materials and 20 mg of carbon black were dispersed in a solution of 3.2 mL (1:1 MilliQ water and ethanol), with 0.2 mL of 10 wt% Nafion solution added. The suspension was sonicated for 1 h, and 10 μL of the resulting ink was drop-cast onto a cleaned GC electrode, and then dried in air. The electrochemical tests were conducted in 1 M KOH, with or without 1 M methanol, using via cyclic voltammetry (CV) and chronoamperometry (CA) techniques. The recorded potential was converted into RHE. Ion chromatography (IC) was performed using an ALiX Lab AS2000 system to analyze the formate products after CA testing.

2.5. DFT Calculations

DFT calculations were performed using the Vienna ab-initio simulation package (VASP). The electron-ion interactions were represented by the projector-augmented wave (PAW) method, and the exchange-correlation interactions were described using the Perdew-Burke-Ernzerhof (PBE) functional within the generalized gradient approximation (GGA) [34,35]. An energy cutoff of 500 eV was applied, and the Brillouin zone was sampled using a 2 × 2 × 1 Monkhorst-Pack k-point mesh. For geometry optimization, the convergence criteria for the electronic and ionic relaxations were set to 1×10^{-5} eV and 0.02 eV $Å^{-1}$, respectively. The DFT-D3 method was applied to take account of the correction of van der Waals interaction. A vacuum layer of 15 Å was introduced along the vertical axis to prevent interactions between adjacent periodic images.

3. Results and Discussion

A series of nickel hydroxide ($Ni(OH)_2$) and iron oxyhydroxide (FeOOH) heterostructures (NFHs) were synthesized using a straightforward hydrothermal method (see experimental section for details). Briefly, precursor solutions containing $NiCl_2 \cdot 6H_2O$, $FeCl_2 \cdot 4H_2O$, urea, and NH_4F were mixed in deionized water and then subjected to hydrothermal treatment at 120 °C for 15 h. The resulting products were washed with water and ethanol, followed by drying at 60 °C for 10 h. Figure 1 shows the XRD profile, matching well with the FeOOH (JCPDS No. 97 003 1136) and $Ni(OH)_2$ (JCPDS No. 00 038 0715) crystal structure. The sustained XRD pattern confirms the successful synthesis of these two structures, even the Ni/Fe ratio was varied in composition according to the adjusted precursor ratios. By varying the nominal molar ratios of Ni/Fe at 3:1, 1:1, and 1:3, the actual Ni/Fe atomic ratios match well with SEM EDS data (Figure S1). In the following, we used the nominal Ni/Fe composition, with $Ni_{0.25}Fe_{0.75}$, $Ni_{0.50}Fe_{0.50}$, and $Ni_{0.75}Fe_{0.25}$, to distinguish these samples.

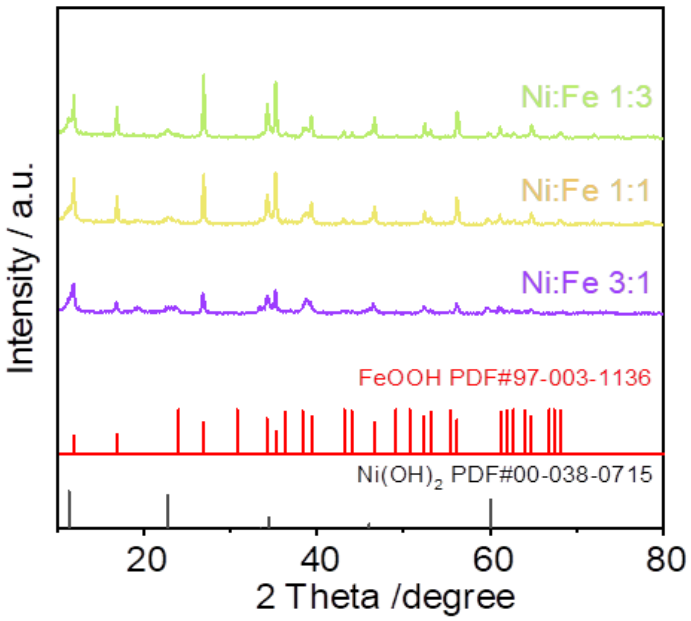

Figure 1. Laboratory XRD patterns for the as-synthesized sample with nominal Ni/Fe atomic ratio of 3/1, 1/1, and 1/3 in the precursors.

Figures 2a and S2 show the obtained NFHs are mainly composed of 3 dimensional (3D) nanoflower-like shapes with an average size of 2–3 μm. As can be seen clearly, the 3D flower morphology composed by nanosheets, and was not obviously changed by tuned Ni/Fe ratio. Figure 2b presents HRTEM image for the NFH based on

$Ni_{0.50}Fe_{0.50}$. In Figure 2c, a plane with a distance of 0.46 nm could be interpreted to $Ni(OH)_2$ (p-3m1) (001) plane. Figure 2d shows Ni and Fe mapping throughout 2 connected flowers. As can be seen clearly, Fe is located in the core, while Ni is more presented in the outer shell. This is consistent with the line scan (Figure 2e), showing the Ni/Fe ratio across a single flower.

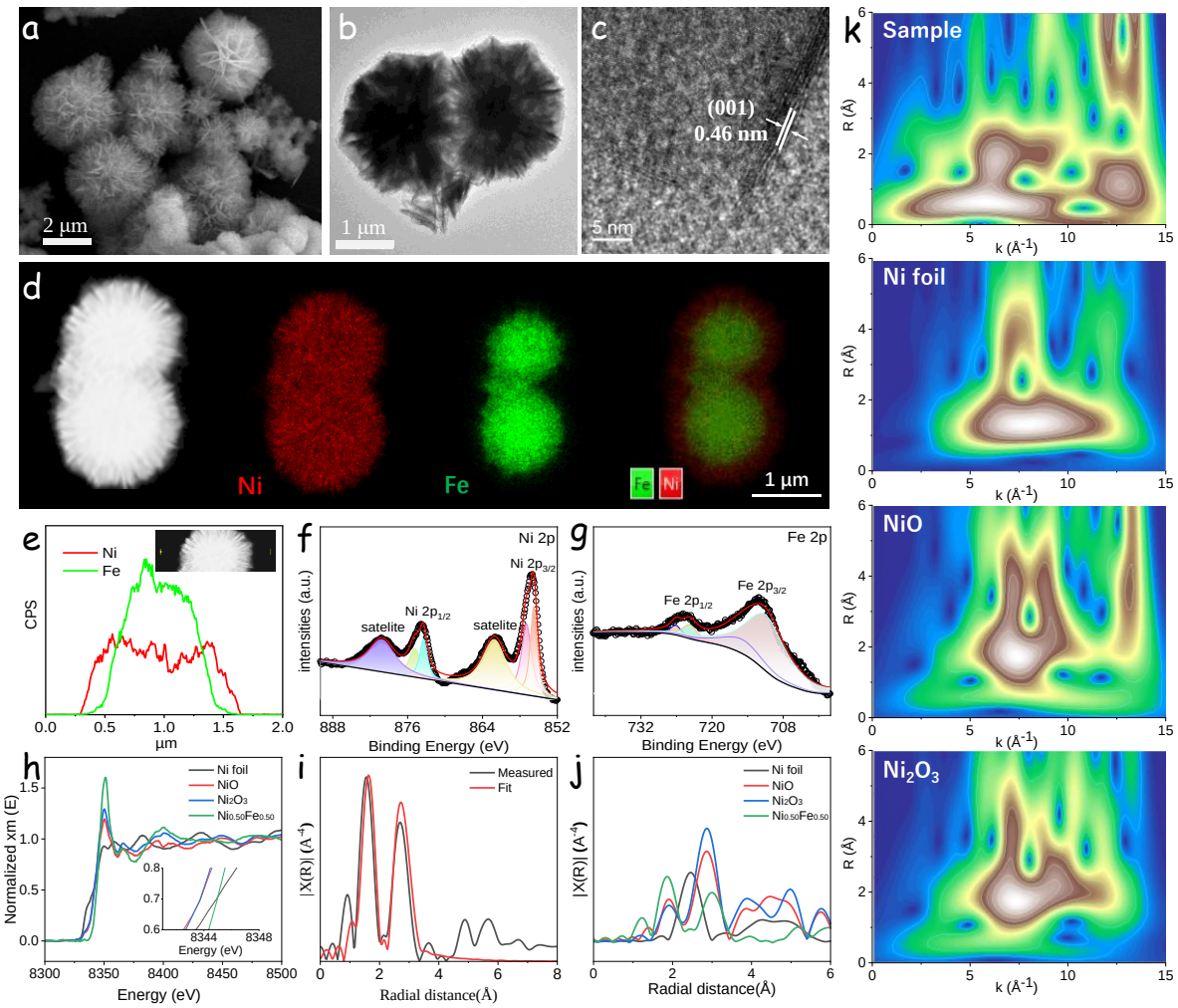

Figure 2. Physical and chemical characterization. (**a**) Representative SEM image for the $Ni_{0.50}Fe_{0.50}$ sample. (**b**,**c**) Corresponding HAADF-STEM image. (**d**) EELS-STEM compositional maps. (**e**) Line scan across a flower. (**f**,**g**) Survey of Ni 2p and Fe 2p XPS spectra. (**h**) Normalized XAFS at the Ni K-edge for the $Ni_{0.5}Fe_{0.5}$-based sample, with Ni_2O_3, NiO, and Ni foil are used as references. (**i**) Experimental and fitting XAFS spectra at the Ni K-edge. (**j**) Normalized XAFS spectra at the Ni K-edge for $Ni_{0.50}Fe_{0.50}$-based sample and the reference. (**k**) Corresponding to WT-XAFS.

The high-resolution XPS of $Ni_{0.5}Fe_{0.5}$-based sample is performed and analyzed to study the surface chemistry. As illustrated in Figure 2f, the Ni 2p XPS spectrum exhibits two satellite peaks at 880.2 eV and 862.1 eV. Another two peaks at 873.9 eV and 856.1 eV can be assigning to Ni^{3+} and Ni^{2+}, respectively. In the high-resolution Fe 2p spectrum (Figure 2g), the fitted peaks for Fe $2p_{3/2}$ and Fe $2p_{1/2}$ was found to be located at approximately 725.1 eV and 712.4 eV. Specifically, the Fe^{3+} was found to locate at 726.2 eV and 716.1 eV, and the Fe^{2+} can be found at 723.8 eV and 711.6 eV, respectively. These characteristics were in good agreements with previous XPS surveys [36–41].

Furthermore, the electronic properties and local chemical environment of the developed materials was performed using XAFS techniques [42]. As can be seen in Figure 2h, the XANES of Ni K-edge indicated that the absorption edge of the $Ni_{0.5}Fe_{0.5}$ sample locates between NiO and Ni_2O_3, demonstrating that the valence of Ni element is between +2 and +3. The EXAFS fitting results indicate that the average valence state of Ni is 2.8, which is in accordance with the results obtained from the above-mentioned XPS. More coordination information of this sample can be obtained by EXAFS fitting, the coordination number of Ni-O andNi-O-Ni are 6.0 and 9.7, respectively. The Ni K-edge Fourier transformed (FT) k3-weighted extended EXAFS spectra (Figure 2i) present

representative peaks at 1.87 and 2.97 Å, corresponding to the NiO bond and the Ni-O-Ni coordination (Figure 2j), respectively. The distinct first-shell Ni-Ni feature characteristic of metallic Ni foil (2.18 Å) was not observed, ruling out the presence of Ni nanoparticles or Ni clusters within this material. The oscillation of the k-space in the pre-edge absorption and the wavelet transform (WT) spectrum of $Ni_{0.5}Fe_{0.5}$ are similar to that of the references, suggesting their similar structures (Figure 2k).

The electrocatalytic performance was evaluated using a traditional three-electrode system, by dropping the catalyst ink on a GC as WE. Firstly, a CV profile was obtained on Ni-Fe-based electrodes, which was tested in the potential range 0.9–1.6 V versus RHE with a scan rate of 50 mV s^{-1} in 1 M KOH electrolyte (Figure 3a). As can be seen in the CV curves, there are two oxidation peaks located at ~1.38 V and ~1.46 V for the electrocatalysts with Ni content higher than 50%, due the formation of NiOOH and FeOOH, respectively [43]. With the increasing content of Fe in the composition, these two peaks overlapped gradually for the most iron-rich NFHs (blue curve in Figure 3a). The rise in the current density in these electrode materials at higher than ca. 1.5 V was associated to the OER [44–47].

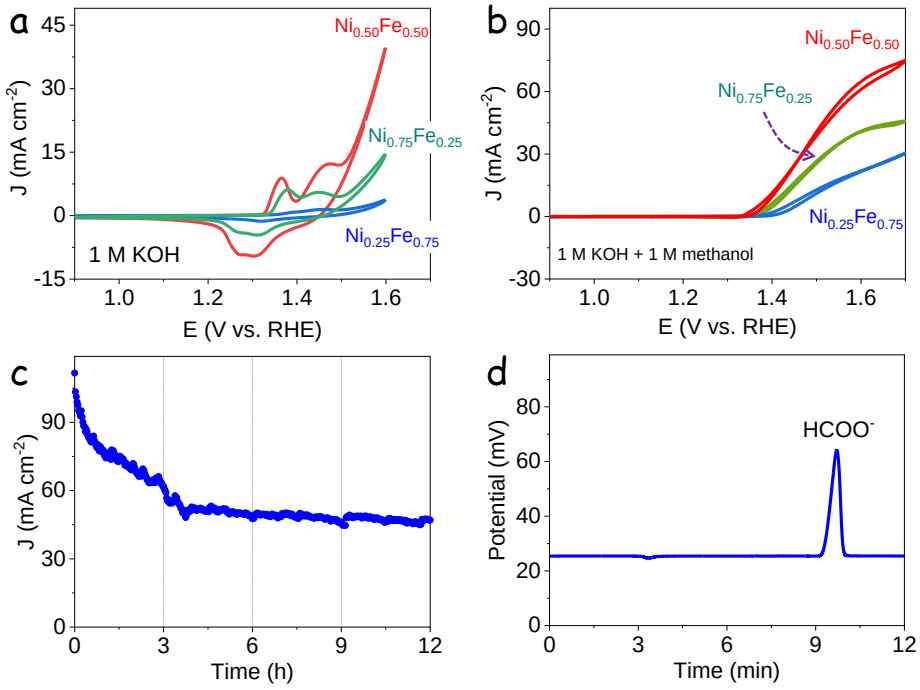

Figure 3. (**a**,**b**) CV curves for the NiFe-based electrodes in an electrolyte containing 1 M KOH solution with or without the presence of 1 M methanol. (**c**) Long-term CA performance for the $Ni_{0.5}Fe_{0.5}$-based electrode at an external potential of 1.6 V versus RHE. (**d**) IC profile for the electrolyte after 12 h CA testing.

Figure 3b presents the CV profile of these three electrodes in 1 M KOH with the addition of 1 M methanol, demonstrating a clear increase in the current density with the rising external potential starting at ~1.4 V. Specifically, at 1.6 V versus RHE, a MOR current density of 42.3, 66.1, and 20.5 mA cm^{-2} was achieved for the NFH electrodes with increasing content of iron, respectively, all higher than that in 1 M KOH with 14.5, 35.6, and 3.7 mA cm^{-2}, respectively. By comparing Figure 3a,b, the larger current density at the same external applied potential demonstrate the electrooxidation of methanol, in good agreement with previous reports on Ni-based electrocatalysts (Table S1). Among these electrocatalysts, the highest MOR performance was obtained on equal Ni/Fe composition.

Figure 3c displays the CA response at external potentials of 1.6 V in the electrolyte consisting of 1 M KOH solution and 1 M methanol. As it can be seen in the curve, a gradual decay of around 45% of the initial current density over the first 4 h was presented, followed by a steady current density of ~50 mA cm^{-2} until 12 h test. At the end of the operation, a little quate of electrolyte was taken and diluted with 20 times MilliQ water, and analyzed with IC. Figure 3d plots the IC profile, demonstrating an obvious upwards peak at 9.7 min. This peak is in good agreement with the characteristics of formate [18]. By fitting with the standardized curve derived from a series of formate concentrations (Figure S2), the actual formate concentration of the electrolyte after 12 h CA operation

was determined to be 2.0 mmol L^{-1}. Thus, 1.2 mmol formate were produced throughout this MOR process. Furthermore, the methanol-to-formate FE was determined using the following equation:

$$FE(\%) = \frac{mol\ of\ product \times n \times F}{total\ charge\ passed} \times 100\%$$

where n is assumed to be 4 for the methanol-to-formate process, and F is the Faradaic constant of 96,485 C mol^{-1}.

Considering the total charge of 471.4 C passed through the electrode, based on the above-equation, the FE was determined to be 98.5% at 1.6 V vs. RHE. The obtained MOR activity and the formate FE is among the top electrocatalysts under the same measurement [11,48,49].

To have a deep understanding between the electronic structure and the MOR performance, the electrochemical behavior was investigated in alkaline media. Among these, the electrochemically active surface area (ECSA) is a critical parameter for evaluating the performance [50]. It is typically determined by measuring the electrochemical double-layer capacitance (C_{dl}) using CVs recorded at various scan rates within the non-faradaic potential range for Ni-based non-precious metal electrocatalysts, as shown in Figure 4a for the $Ni_{0.50}Fe_{0.50}$ based electrode. As illustrated in Figure 4b, plotting the charging current against the scan rate yields a linear relationship. The slope corresponds to C_{dl} for the $Ni_{0.50}Fe_{0.50}$-based electrode (Figure 4b). Furthermore, the ECSA value can then be derived using the following equation:

$$ECSA = C_{dl}/C_s$$

where C_s represents the specific capacitance, typically assumed to be 0.04 mF cm^{-2} for metal electrodes in aqueous NaOH solution [8]. Based on this, the ECSA values were calculated to be 17.4 $cm^2\ g^{-1}$ (Figure S4), 38.8 $cm^2\ g^{-1}$, and 15.5 $cm^2\ g^{-1}$ (Figure S5), respectively. These values were presented and compared in Figure 4c.

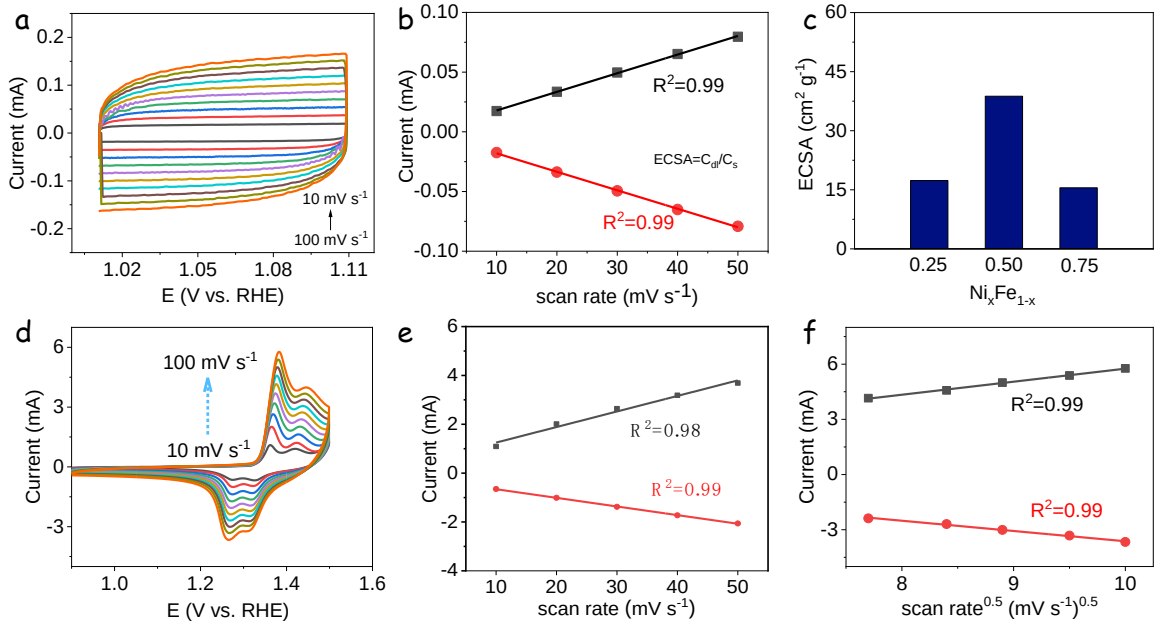

Figure 4. (**a**) CVs of the $Ni_{0.50}Fe_{0.50}$-based electrode in the double-layer region at variable scan rates ranging from 10 to 100 mV s^{-1} in 1 M KOH. (**b**) Linear relationship between capacitive current density and scan rate. (**c**) Calculated ECSA for the NFHs. (**d**) CVs of the $Ni_{0.50}Fe_{0.50}$-based electrode in 1 M KOH at a fixed scan rate of 50 mV s^{-1}. (**e**) Linear fitting of anodic and cathodic peak current densities versus scan rate range from 10 to 50 mV s^{-1}. (**f**) Linear fitting of anodic and cathodic peak current densities versus the square root of scan rate range from 60 to100 mV s^{-1}.

As shown in Figure 4d, increasing the scan rate resulted in a shift of the anodic peak to higher potentials and the cathodic peak to lower potentials for the $Ni_{0.50}Fe_{0.50}$-based electrode in 1 M KOH. A similar pattern was obtained for the other two compositions (Figures S6a and S7a). Figure 4e displays the current densities of both the anodic and cathodic peaks, exhibiting a linear increase with the scan rate. The surface coverage of redox species (Γ^*) was estimated from the average slope of the anodic and cathodic peaks versus the scan rate (v) using the equation [51]:

$$I_p = \left(\frac{n^2F^2}{4RT}\right)A\Gamma^* v$$

Where n is assumed to be 1 as the number of transferred electrons, F is the Faraday constant (96,485 C mol^{-1}), R is the gas constant (8.314 J K^{-1} mol^{-1}), T is the temperature, and A is the geometric surface area of the GC electrode (0.196 cm^2).

Using this equation, the Γ^* values were determined to be 2.53 × 10^{-7} mol cm^{-2} (Figure S6b), 2.69 × 10^{-7} mol cm^{-2} (Figure 4e), and 9.47 × 10^{-8} mol cm^{-2} (Figure S7b) for the NFHs-based electrodes with rising Fe-content, respectively.

Additionally, as shown in Figure 4f, a linear relationship was observed between the peak current density and the square root of the scan rate for the three electrodes in 1 M KOH. This relationship is indicative of a diffusion-limited $Ni(OH)_2$/NiOOH redox reaction, where proton diffusion within the particle is the rate-limiting step. The relationship is expressed as [51]:

$$I_p = 2.69 \times 10^5 n^{3/2} A D^{1/2} C v^{1/2}$$

where I_p is the peak current, D is the diffusion coefficient, C is the proton concentration (estimated at 0.043 mol cm^{-3}), and v is the scan rate. By fitting the peak current to the square root of the scan rate, the D were calculated to be 3.02 × 10^{-9} cm^2 s^{-1} for the $Ni_{0.50}Fe_{0.50}$-based electrode, higher than the $Ni_{0.25}Fe_{0.75}$-based electrode with 2.25 × 10^{-9} cm^2 s^{-1} (Figure S6c) and 4.34 × 10^{-10} cm^2 s^{-1} (Figure S7c). The higher MOR electrocatalytic performance was highly related to the enhanced intrinsic property with the proper Ni/Fe ratio in the heterostructures.

Aparting from the intrinsic property, further DFT calculations were usually performed to gain further insight into the MOR reaction mechanism [52–54]. Three different compositions of Ni/Fe in NiFeOOH are considered: $Ni_{0.75}Fe_{0.25}OOH$, $Ni_{0.50}Fe_{0.50}OOH$, and $Ni_{0.25}Fe_{0.75}OOH$. Figure 5a,b present the corresponding partial density of state (PDOS) derived from DFT calculations. As can be seen clearly in the figure, the d electrons (ε_d) of NiFe in NiFeOOH were determined to be −1.64 eV, −1.56 eV and −1.41 eV with the increasing iron content in the sample. A similar trend of ε_d of Ni was calculated, increasing from −1.68 eV for $Ni_{0.75}Fe_{0.25}OOH$ to −1.61 eV for $Ni_{0.50}Fe_{0.50}OOH$, and to −1.53 eV for $Ni_{0.25}Fe_{0.75}OOH$. The d electrons concentrate more around the Fermi level, and can be effectively tailored by the Ni/Fe ratio, leading to an enhancement of the electroconductivity and electron transfer [55–58].

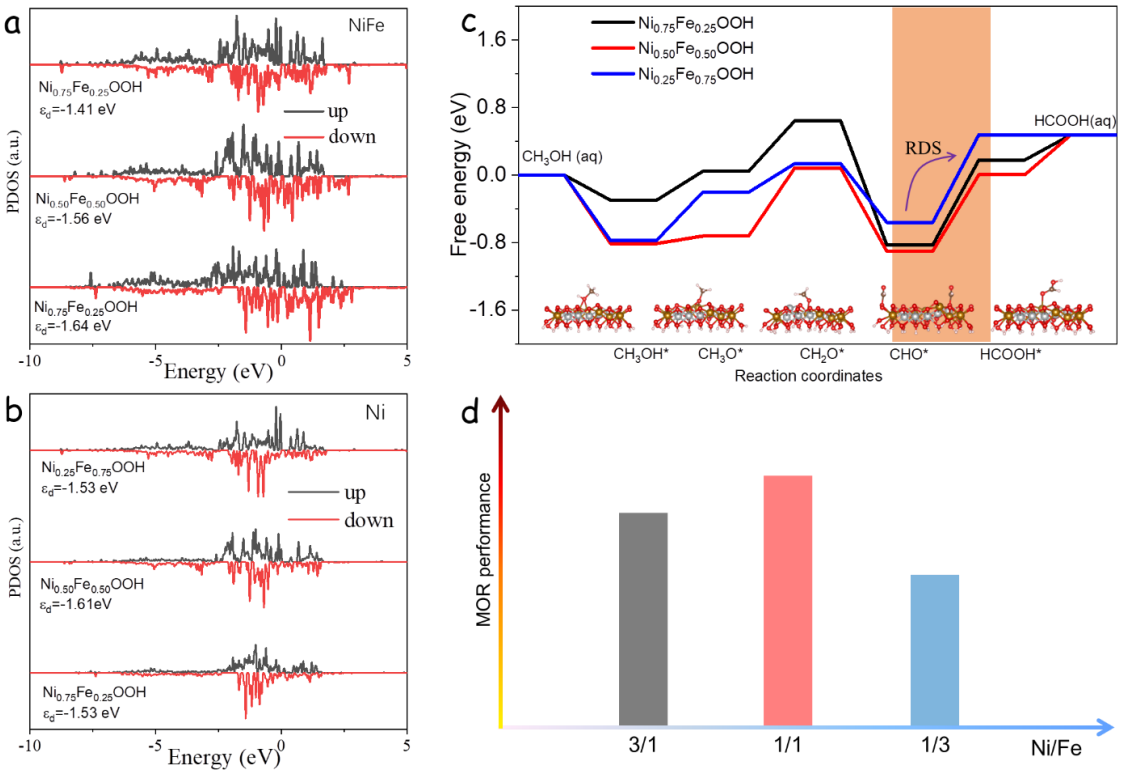

Figure 5. (**a**,**b**) PDOS of the NFHs in the NiFe and Ni. (**c**) Gibbs free energy diagrams for the methanol-to-formate conversion on NiFeOOH surfaces, and the optimized adsorbed intermediates on the surfaces. (**d**) Relationship between the MOR electrocatalytic performance and the Ni/Fe atomic ratio.

In the calculation of the adsorption energy of several intermediate, including CH_3OH*, CH_3O*, CH_2O*, CHO*, and HCOOH*, during the methanol-to-formate process [52], the (001) facet of these three models was chosen. The Gibbs free energy profile, as shown in Figure 5c, exhibits fluctuations as the reaction proceeds through these intermediates. Specifically, the adsorption energy for methanol from gaseous phase is enhanced by the increasing content of iron, with −0.298 eV for $Ni_{0.25}Fe_{0.75}OOH$, −0.812 eV for $Ni_{0.50}Fe_{0.50}OOH$, and −0.775 eV for $Ni_{0.25}Fe_{0.75}OOH$, respectively. At the first two hydrogenation step to CH_2O* is energetically upwards, but the final dehydrogenation step forming CHO* is exothermal. After the dehydrogenations, the formed CHO* interacts with the surrounding hydroxide ion by forming HCOOH, and then released from the surface, and finally exists as formate in the alkaline media. By comparing the free energy landscape, the MOR rate-limiting step was from CHO*to HCOOH*, with an energy barrier of 0.90 eV for $Ni_{0.50}Fe_{0.50}OOH$, lower than the 1.01 eV for $Ni_{0.75}Fe_{0.25}OOH$, and 1.04 eV for $Ni_{0.25}Fe_{0.75}OOH$, respectively.

Overall, the DFT results were consistent with the experimental findings in the MOR following the order of $Ni_{0.50}Fe_{0.50}$, $Ni_{0.75}Fe_{0.25}$ and $Ni_{0.25}Fe_{0.75}$ (Figure 5d). Additionally, the higher MOR performance was highly related to the improved intrinsic property, including ECSA, active surface coverage, and diffusivity of redox pairs, arising from the Ni/Fe ratio in the NFHs.

4. Conclusions

In summary, this work reports nickel hydroxide and iron oxyhydroxide heterostructures with 3D flower morphology using a facile hydrothermal method. The prepared electrode materials were characterized, and their catalytic MOR performance in alkaline solution was evaluated and optimized with Ni/Fe ratio. In addition, the improved performance was highly associated to the ECSA, surface coverage of active species, and diffusion coefficient. Moreover, the methanol-to-formate FE was found to be close to 100%. Furthermore, DFT calculation suggests that the RDS was in the CHO*-HCOOH* step and the energy barrier was reduced by the proper iron presence in the electrode. These results showcase the high methanol-to-formate efficiency over NiFe-based materials, offering a promising option of a non-precious catalyst for the anodic electrocatalytic upgrading of methanol into value-added formate products.

Supplementary Materials: The following supporting information can be downloaded at: https://www.sciltp.com/journals/see/2025/1/873/s1, Figure S1: SEM-EDS results for the samples obtained from Ni/Fe ratio with (a) 3:1, (b) 1:1, and (c) 1:3 in the precursor. Figure S2: Representative SEM images for (a) $Ni_{0.75}Fe_{0.25}$ and (b) $Ni_{0.25}Fe_{0.75}$ based NFHs. Figure S3: Standard IC profile for formate concentration and the corresponding fiting formate peak area and concentration. Figure S4: Determination of ECSA curves in 1 M KOH for the $Ni_{0.75}Fe_{0.25}$-based electrode. Figure S5: Determination of ECSA curves in 1 M KOH for the $Ni_{0.25}Fe_{0.75}$-based electrode. Figure S6: Intrinsic property for the $Ni_{0.75}Fe_{0.25}$-based electrode in 1 M KOH (a) CVs, (b) surface coverage of redox species (Γ*), and (c) diffusion coefficient (D). Figure S7: Intrinsic property for the $Ni_{0.25}Fe_{0.75}$-based electrode in 1 M KOH (a) CVs, (b) surface coverage of redox species (Γ*), and (c) diffusion coefficient (D).; Table S1: Comparison of MOR performance between this work and previously published noble-metal-free electrocatalysts. References [59–66] are cited in the supplementary materials.

Author Contributions: N.J. conceptualization, methodology, writing—original draft preparation; H.G.: data curation; Y.M.: data curation, investigation; Y.Z.: data curation; L.L.: data curation, visualization, investigation; J.L. (Junfeng Liu): data curation, validation; J.Y. data curation, investigation; C.L.: data curation, investigation, J.L. (Junshan Li): supervision, writing—reviewing and editing. All authors have read and agreed to the published version of the manuscript.

Funding: This work was supported by the Natural Science Foundation of Sichuan province (2025ZNSFSC0139), and also by the China Postdoctoral Science Foundation under Grant Number 2023MD734228.

Institutional Review Board Statement: Not applicable.

Informed Consent Statement: Not applicable.

Data Availability Statement: All the research data associated to this manuscript have been included as a part of the Supplementary Information.

Conflicts of Interest: The authors declare no competing financial interest.

References

1. Campos-Seijo, B. Carbon-Neutrality Goals. *C&EN Glob. Enterp.* **2020**, *98*, 4. https://doi.org/10.1021/cen-09840-editorial.
2. Liu, C.; Li, F.; Lai-Peng, M.; Cheng, H.M. Advanced Materials for Energy Storage. *Adv. Mater.* **2010**, *22*, E28–E62. https://doi.org/10.1002/adma.200903328.

3. Yadav, V.G.; Yadav, G.D.; Patankar, S.C. The Production of Fuels and Chemicals in the New World: Critical Analysis of the Choice between Crude Oil and Biomass Vis-à-Vis Sustainability and the Environment. *Clean Technol. Environ. Policy* **2020**, *22*, 1757–1774. https://doi.org/10.1007/s10098-020-01945-5.
4. Turner, J.A. Sustainable Hydrogen Production. *Science* **2004**, *305*, 972–974. https://doi.org/10.1126/science.1103197.
5. Wang, P.; Zhang, R.; Wang, K.; Liu, Y.; Zhang, L.; Wang, X.; Li, H.; He, Y.; Liu, Z. Simultaneously Constructing Asymmetrically Coordinated Cobalt Single Atoms and Cobalt Nanoclusters via a Fresh Potassium Hydroxide Clipping Strategy toward Efficient Alkaline Oxygen Reduction Reaction. *Energy Mater. Adv.* **2023**, *4*, 0042. https://doi.org/10.34133/energymatadv.0042.
6. Moges, E.A.; Lakshmanan, K.; Chang, C.Y.; Liao, W.S.; Angerasa, F.T.; Dilebo, W.B.; Edao, H.G.; Tadele, K.T.; Alemayehu, D.D.; Bejena, B.D.; et al. Materials of Value-Added Electrolysis for Green Hydrogen Production. *ACS Mater. Lett.* **2024**, *6*, 4932–4954. https://doi.org/10.1021/acsmaterialslett.4c01173.
7. Moges, E.A.; Chang, C.Y.; Tsai, M.C.; Su, W.N.; Hwang, B.J. Electrocatalysts for Value-Added Electrolysis Coupled with Hydrogen Evolution. *EES Catal.* **2023**, *1*, 413–433. https://doi.org/10.1039/d3ey00017f.
8. McCrory, C.C.L.; Jung, S.; Ferrer, I.M.; Chatman, S.M.; Peters, J.C.; Jaramillo, T.F. Benchmarking Hydrogen Evolving Reaction and Oxygen Evolving Reaction Electrocatalysts for Solar Water Splitting Devices. *J. Am. Chem. Soc.* **2015**, *137*, 4347–4357. https://doi.org/10.1021/ja510442p.
9. Stamenkovic, V.R.; Strmcnik, D.; Lopes, P.P.; Markovic, N.M. Energy and Fuels from Electrochemical Interfaces. *Nat. Mater.* **2016**, *16*, 57–69. https://doi.org/10.1038/nmat4738.
10. Xiang, K.; Wu, D.; Deng, X.; Li, M.; Chen, S.; Hao, P.; Guo, X.; Luo, J.L.; Fu, X.Z. Boosting H2 Generation Coupled with Selective Oxidation of Methanol into Value-Added Chemical over Cobalt Hydroxide@Hydroxysulfide Nanosheets Electrocatalysts. *Adv. Funct. Mater.* **2020**, *30*, 1909610. https://doi.org/10.1002/adfm.201909610.
11. Li, J.; Li, L.; Wang, J.; Cabot, A.; Zhu, Y. Boosting Hydrogen Evolution by Methanol Oxidation Reaction on Ni-Based Electrocatalysts: From Fundamental Electrochemistry to Perspectives. *ACS Energy Lett.* **2024**, *9*, 853–879. https://doi.org/10.1021/acsenergylett.3c02678.
12. Ren, J.; Zhang, Y.; Li, J.; Liu, J.; Hu, J.; Li, C.; Ke, Y.; Zhao, J.; Cabot, A.; Tang, B. Hydrothermal Nickel Selenides as Efficient Electrodes in Alkaline Media: Application to Supercapacitors and Methanol Oxidation Reaction. *Dalt. Trans.* **2024**, *53*, 18736–18744. https://doi.org/10.1039/D4DT02472A.
13. Ma, Y.; Li, L.; Tang, J.; Hu, Z.; Zhang, Y.; Ge, H.; Jian, N.; Zhao, J.; Cabot, A.; Li, J. Electrochemical PET Recycling to Formate through Ethylene Glycol Oxidation on Ni-Co-S Nanosheet Arrays. *J. Mater. Chem. A* **2024**, *12*, 33917–33925. https://doi.org/10.1039/d4ta07156e.
14. Zhang, Y.; Liu, R.; Ma, Y.; Jian, N.; Pan, H.; Liu, Y.; Deng, J.; Li, L.; Shao, Q.; Li, C.; et al. Nickel-Cobalt Oxide Nanoparticles as Superior Electrocatalysts for Enhanced Coupling Hydrogen Evolution and Selective Ethanol Oxidation Reaction. *J. Mater. Chem. A* **2024**, *12*, 17252–17259. https://doi.org/10.1039/d4ta03259d.
15. Kakati, N.; Maiti, J.; Lee, S.H.; Jee, S.H.; Viswanathan, B.; Yoon, Y.S. Anode Catalysts for Direct Methanol Fuel Cells in Acidic Media: Do We Have Any Alternative for Pt or Pt-Ru? *Chem. Rev.* **2014**, *114*, 12397–12429. https://doi.org/10.1021/cr400389f.
16. Wu, D.; Hao, J.; Song, Z.; Fu, X.Z.; Luo, J.L. All Roads Lead to Rome: An Energy-Saving Integrated Electrocatalytic CO_2 Reduction System for Concurrent Value-Added Formate Production. *Chem. Eng. J.* **2020**, *412*, 127893. https://doi.org/10.1016/j.cej.2020.127893.
17. Liu, Y.P.; Zhao, S.F.; Guo, S.X.; Bond, A.M.; Zhang, J.; Zhu, G.; Hill, C.L.; Geletii, Y.V. Electrooxidation of Ethanol and Methanol Using the Molecular Catalyst $[\{Ru_4O_4(OH)_2(H2O)_4\}(\gamma\text{-}SiW_{10}O_{36})_2]^{10-}$. *J. Am. Chem. Soc.* **2016**, *138*, 2617–2628. https://doi.org/10.1021/jacs.5b11408.
18. Zhang, Y.; Liu, R.; Ma, Y.; Jian, N.; Ge, H.; Pan, H.; Zhang, Y.; Zhang, C.; Liu, Y.; Deng, J.; et al. Surface Selenium Coating Promotes Selective Methanol-to-Formate Electrooxidation on Ni3Se4 Nanoparticles. *Inorg. Chem.* **2024**, *63*, 23328–23337. https://doi.org/10.1021/acs.inorgchem.4c03996.
19. Yi, Y.; Li, J.; Cui, C. Trimetallic FeCoNi Disulfide Nanosheets for CO_2-Emission-Free Methanol Conversion. *Chinese Chem. Lett.* **2022**, *33*, 1006–1010. https://doi.org/10.1016/j.cclet.2021.07.005.
20. Liu, J.; Li, T.; Wang, Q.; Liu, H.; Wu, J.; Sui, Y.; Li, H.; Tang, P.; Wang, Y. Bifunctional PdMoPt Trimetallene Boosts Alcohol-Water Electrolysis. *Chem. Sci.* **2024**, *15*, 16660–16668. https://doi.org/10.1039/d4sc04764h.
21. Liu, H.; Li, T.; Wu, Z.; Xu, H.; Li, H.; Jing, R.; Wang, Y.; Liu, J. Integration of Phosphorus in PdCr Metallene for Enhanced CO-Tolerant Alcohol Electrooxidation. *Inorg. Chem.* **2024**, *64*, 123–132. https://doi.org/10.1021/acs.inorgchem.4c04334.
22. Liu, J.; Liu, H.; Wang, Q.; Li, T.; Yang, T.; Zhang, W.; Xu, H.; Li, H.; Qi, X.; Wang, Y.; et al. Phosphorus Doped PdMo Bimetallene as a Superior Bifunctional Fuel Cell Electrocatalyst. *Chem. Eng. J.* **2024**, *486*, 150258. https://doi.org/10.1016/j.cej.2024.150258.

23. Liu, J.; Wang, Q.; Li, T.; Wang, Y.; Li, H.; Cabot, A. PdMoSb Trimetallene as High-Performance Alcohol Oxidation Electrocatalyst. *Nano Res.* **2023**, *16*, 2041–2048. https://doi.org/10.1007/s12274-022-4873-8.
24. Zhou, J.; Yuan, L.; Wang, J.; Song, L.; You, Y.; Zhou, R.; Zhang, J.; Xu, J. Combinational Modulations of $NiSe_2$ Nanodendrites by Phase Engineering and Iron-Doping towards an Efficient Oxygen Evolution Reaction. *J. Mater. Chem. A* **2020**, *8*, 8113–8120. https://doi.org/10.1039/d0ta00860e.
25. Chen, D.; Minteer, S.D. Mechanistic Study of Nickel Based Catalysts for Oxygen Evolution and Methanol Oxidation in Alkaline Medium. *J. Power Sources* **2015**, *284*, 27–37. https://doi.org/10.1016/j.jpowsour.2015.02.143.
26. Zhang, M.; Zhu, J.; Wan, R.; Liu, B.; Zhang, D.; Zhang, C.; Wang, J.; Niu, J. Synergistic Effect of Nickel Oxyhydroxide and Tungsten Carbide in Electrocatalytic Alcohol Oxidation. *Chem. Mater.* **2022**, *34*, 959–969. https://doi.org/10.1021/acs.chemmater.1c02535.
27. Kowal, A.; Port, S.N.; Nichols, R.J. Nickel Hydroxide Electrocatalysts for Alcohol Oxidation Reactions: An Evaluation by Infrared Spectroscopy and Electrochemical Methods. *Catal. Today* **1997**, *38*, 483–492. https://doi.org/10.1016/S0920-5861(97)00049-7.
28. Bender, M.T.; Lam, Y.C.; Hammes-Schiffer, S.; Choi, K.S. Unraveling Two Pathways for Electrochemical Alcohol and Aldehyde Oxidation on NiOOH. *J. Am. Chem. Soc.* **2021**, *142*, 21538–21547. https://doi.org/10.1021/jacs.0c10924.
29. Wang, T.J.; Huang, H.; Wu, X.R.; Yao, H.C.; Li, F.M.; Chen, P.; Jin, P.J.; Deng, Z.W.; Chen, Y. Selflate Synthesis of Defect-Rich NiO Nanotubes as Efficient Electrocatalysts for Methanol Oxidation Reaction. *Nanoscale* **2019**, *11*, 19783–19790. https://doi.org/10.1039/c9nr06304h.
30. Xu, Y.; Liu, M.; Wang, M.; Ren, T.; Ren, K.; Wang, Z.; Li, X.; Wang, L.; Wang, H. Methanol Electroreforming Coupled to Green Hydrogen Production over Bifunctional NiIr-Based Metal-Organic Framework Nanosheet Arrays. *Appl. Catal. B Environ.* **2022**, *300*, 120753. https://doi.org/10.1016/j.apcatb.2021.120753.
31. Li, J.; Ma, Y.; Yu, J.; Li, L.; Yang, H.; Gu, W.; Shi, J.; Wang, J.; Zhu, Y. Enhanced Methanol Electrooxidation and Supercapacitive Performance via Compositional Engineering of Colloidal Ni-Co Alloying Nanoparticles. *ChemSusChem* **2024**, *18*, e202401098. https://doi.org/10.1002/cssc.202401098.
32. Ma, Y.; Li, L.; Zhang, Y.; Jian, N.; Pan, H.; Deng, J.; Li, J. Nickel Foam Supported Mn-Doped NiFe-LDH Nanosheet Arrays as Efficient Bifunctional Electrocatalysts for Methanol Oxidation and Hydrogen Evolution. *J. Colloid Interface Sci.* **2024**, *663*, 971–980. https://doi.org/10.1016/j.jcis.2024.02.191.
33. Li, J.; Xing, C.; Zhang, Y.; Zhang, T.; Spadaro, M.C.; Wu, Q.; Yi, Y.; He, S.; Llorca, J.; Arbiol, J.; et al. Nickel Iron Diselenide for Highly Efficient and Selective Electrocatalytic Conversion of Methanol to Formate. *Small* **2021**, *17*, 2006623. https://doi.org/10.1002/smll.202006623.
34. Perdew, J.P.; Burke, K.; Ernzerhof, M. Generalized Gradient Approximation Made Simple. *Phys. Rev. Lett.* **1996**, *77*, 3865–3868. https://doi.org/10.1103/PhysRevLett.77.3865.
35. Kresse, G.; Furthmüller, J. Efficient Iterative Schemes for Ab Initio Total-Energy Calculations Using a Plane-Wave Basis Set. *Phys. Rev. B-Condens. Matter Mater. Phys.* **1996**, *54*, 11169–11186. https://doi.org/10.1103/PhysRevB.54.11169.
36. Meng, F.; Wu, Q.; Elouarzaki, K.; Luo, S.; Sun, Y.; Dai, C.; Xi, S.; Chen, Y.; Lin, X.; Fang, M.; et al. Essential Role of Lattice Oxygen in Methanol Electrochemical Refinery toward Formate. *Sci. Adv.* **2023**, *9*, eadh9487. https://doi.org/10.1126/sciadv.adh9487.
37. Zhou, H.; Ren, Y.; Li, Z.; Xu, M.; Wang, Y.; Ge, R.; Kong, X.; Zheng, L.; Duan, H. Electrocatalytic Upcycling of Polyethylene Terephthalate to Commodity Chemicals and H2 Fuel. *Nat. Commun.* **2021**, *12*, 4679. https://doi.org/10.1038/s41467-021-25048-x.
38. Friebel, D.; Louie, M.W.; Bajdich, M.; Sanwald, K.E.; Cai, Y.; Wise, A.M.; Cheng, M.J.; Sokaras, D.; Weng, T.C.; Alonso-Mori, R.; et al. Identification of Highly Active Fe Sites in (Ni,Fe)OOH for Electrocatalytic Water Splitting. *J. Am. Chem. Soc.* **2015**, *137*, 1305–1313. https://doi.org/10.1021/ja511559d.
39. Feng, X.; Liu, B.W.; Guo, K.X.; Fan, L.F.; Wang, G.X.; Ci, S.Q.; Wen, Z.H. Anodic Electrocatalysis of Glycerol Oxidation for Hybrid Alkali/Acid Electrolytic Hydrogen Generation. *J. Electrochem.* **2023**, *29*, 1–10. https://doi.org/10.13208/j.electrochem.2215005.
40. Chen, J.; Wang, K.; Liu, Z.; Sun, X.; Zhang, X.; Lei, F.; Wan, X.; Xie, J.; Tang, B. Sulfurization-Induced Lattice Disordering in High-Entropy Catalyst for Promoted Bifunctional Electro-Oxidation Behavior. *Chem. Eng. J.* **2024**, *489*, 151234. https://doi.org/10.1016/j.cej.2024.151234.
41. Li, J.; Yu, J.; Zhang, Y.; Li, C.; Ma, Y.; Ge, H.; Jian, N.; Li, L.; Zhang, C.Y.; Zhou, J.Y.; et al. Boosting Polysulfide Conversion on Fe-Doped Nickel Diselenide Toward Robust Lithium–Sulfur Batteries. *Adv. Funct. Mater.* **2025**, 2501485. https://doi.org/10.1002/ADFM.202501485.
42. Li, H.H.; Xie, M.L.; Cui, C.H.; He, D.; Gong, M.; Jiang, J.; Zheng, Y.R.; Chen, G.; Lei, Y.; Yu, S.H. Surface Charge Polarization at the Interface: Enhancing the Oxygen Reduction via Precise Synthesis of Heterogeneous Ultrathin Pt/PtTe Nanowire. *Chem. Mater.* **2016**, *28*, 8890–8898. https://doi.org/10.1021/acs.chemmater.6b02769.

43. Trotochaud, L.; Young, S.L.; Ranney, J.K.; Boettcher, S.W. Nickel-Iron Oxyhydroxide Oxygen-Evolution Electrocatalysts: The Role of Intentional and Incidental Iron Incorporation. *J. Am. Chem. Soc.* **2014**, *136*, 6744–6753. https://doi.org/10.1021/ja502379c.
44. Phan, V.T.T.; Nguyen, Q.P.; Wang, B.; Burgess, I.J. Oxygen Vacancies Alter Methanol Oxidation Pathways on NiOOH. *J. Am. Chem. Soc.* **2024**, *146*, 4830–4841. https://doi.org/10.1021/jacs.3c13222.
45. Zhao, B.; Liu, J.; Xu, C.; Feng, R.; Sui, P.; Luo, J.X.; Wang, L.; Zhang, J.; Luo, J.L.; Fu, X.Z. Interfacial Engineering of Cu2Se/Co3Se4 Multivalent Hetero-Nanocrystals for Energy-Efficient Electrocatalytic Co-Generation of Value-Added Chemicals and Hydrogen. *Appl. Catal. B Environ.* **2021**, *285*, 119800. https://doi.org/10.1016/j.apcatb.2020.119800.
46. Zhan, C.; Bu, L.; Sun, H.; Huang, X.; Zhu, Z.; Yang, T.; Ma, H.; Li, L.; Wang, Y.; Geng, H.; et al. Medium/High-Entropy Amalgamated Core/Shell Nanoplate Achieves Efficient Formic Acid Catalysis for Direct Formic Acid Fuel Cell. *Angew. Chem.-Int. Ed.* **2023**, *62*, 1–8. https://doi.org/10.1002/anie.202213783.
47. Cao, C.; Ma, D.D.; Jia, J.; Xu, Q.; Wu, X.T.; Zhu, Q.L. Divergent Paths, Same Goal: A Pair-Electrosynthesis Tactic for Cost-Efficient and Exclusive Formate Production by Metal–Organic-Framework-Derived 2D Electrocatalysts. *Adv. Mater.* **2021**, *33*, 2008631. https://doi.org/10.1002/adma.202008631.
48. Deng, X.; Li, M.; Fan, Y.; Wang, L.; Fu, X.Z.; Luo, J.L. Constructing Multifunctional 'Nanoplatelet-on-Nanoarray' Electrocatalyst with Unprecedented Activity towards Novel Selective Organic Oxidation Reactions to Boost Hydrogen Production. *Appl. Catal. B Environ.* **2020**, *278*, 119339. https://doi.org/10.1016/j.apcatb.2020.119339.
49. Hao, J.; Liu, J.; Wu, D.; Chen, M.; Liang, Y.; Wang, Q.; Wang, L.; Fu, X.Z.; Luo, J.L. In Situ Facile Fabrication of Ni(OH)2 Nanosheet Arrays for Electrocatalytic Co-Production of Formate and Hydrogen from Methanol in Alkaline Solution. *Appl. Catal. B Environ.* **2021**, *281*, 119510. https://doi.org/10.1016/j.apcatb.2020.119510.
50. Wei, C.; Sun, S.; Mandler, D.; Wang, X.; Qiao, S.Z.; Xu, Z.J. Approaches for Measuring the Surface Areas of Metal Oxide Electrocatalysts for Determining Their Intrinsic Electrocatalytic Activity. *Chem. Soc. Rev.* **2019**, *48*, 2518–2534. https://doi.org/10.1039/c8cs00848e.
51. Bard, A.J.; Faulkner, L.R. *Electrochemical Methods: Fundamentals and Applications*, 2nd ed.; John Wiley & Sons: Hoboken, NJ, USA, 2001.
52. Zhao, B.; Liu, J.; Wang, X.; Xu, C.; Sui, P.; Feng, R.; Wang, L.; Zhang, J.; Luo, J.L.; Fu, X.Z. CO_2-Emission-Free Electrocatalytic CH_3OH Selective Upgrading with High Productivity at Large Current Densities for Energy Saved Hydrogen Co-Generation. *Nano Energy* **2021**, *80*, 105530. https://doi.org/10.1016/j.nanoen.2020.105530.
53. Sun, S.N.; Dong, L.Z.; Li, J.R.; Shi, J.W.; Liu, J.; Wang, Y.R.; Huang, Q.; Lan, Y.Q. Redox-Active Crystalline Coordination Catalyst for Hybrid Electrocatalytic Methanol Oxidation and CO2 Reduction. *Angew. Chem.-Int. Ed.* **2022**, *61*, e202207282. https://doi.org/10.1002/anie.202207282.
54. Ganguly, S.; Paul, S.; Khurana, D.; Khan, T.S.; Giri, P.K.; Loha, C.; Ghosh, S. Ternary Ni-Co-Se Nanostructure for Electrocatalytic Oxidative Value Addition of Biomass Platform Chemicals. *ACS Appl. Energy Mater.* **2023**, *6*, 5331–5341. https://doi.org/10.1021/acsaem.3c00313.
55. Liu, B.; Wang, X.; Wang, S.; Peng, H.Q.; Xiao, T.; Liu, G.; Bai, S.; Zhao, Y.; Zhang, W.; Song, Y.F. Hydroxyl Vacancies Triggered High Methanol Oxidation Activity of Monolayered Layered Double Hydroxides for Energy-Saving Hydrogen Production. *Mater. Today Energy* **2022**, *28*, 101082. https://doi.org/10.1016/j.mtener.2022.101082.
56. Schimpf, A.M.; Knowles, K.E.; Carroll, G.M.; Gamelin, D.R. Electronic Doping and Redox-Potential Tuning in Colloidal Semiconductor Nanocrystals. *Acc. Chem. Res.* **2015**, *48*, 1929–1937. https://doi.org/10.1021/acs.accounts.5b00181.
57. Si, F.; Liu, J.; Zhang, Y.; Zhao, B.; Liang, Y.; Wu, X.; Kang, X.; Yang, X.; Zhang, J.; Fu, X.Z.; et al. Surface Spin Enhanced High Stable $NiCo_2S_4$ for Energy-Saving Production of H_2 from Water/Methanol Coelectrolysis at High Current Density. *Small* **2023**, *19*, 2205257. https://doi.org/10.1002/smll.202205257.
58. Li, J.; Li, L.; Ma, X.; Han, X.; Xing, C.; Qi, X.; He, R.; Arbiol, J.; Pan, H.; Zhao, J.; et al. Selective Ethylene Glycol Oxidation to Formate on Nickel Selenide with Simultaneous Evolution of Hydrogen. *Adv. Sci.* **2023**, *10*, 2300841. https://doi.org/10.1002/advs.202300841.
59. Abdullah, M.I.; Hameed, A.; Zhang, N.; Islam, M.H.; Ma, M.; Pollet, B.G. Ultrasonically Surface-Activated Nickel Foam as a Highly Efficient Monolith Electrode for the Catalytic Oxidation of Methanol to Formate. *ACS Appl. Mater. Interfaces* **2021**, *13*, 30603–30613. https://doi.org/10.1021/acsami.1c06258.
60. Mondal, B.; Karjule, N.; Singh, C.; Shimoni, R.; Volokh, M.; Hod, I.; Shalom, M. Unraveling the Mechanisms of Electrocatalytic Oxygenation and Dehydrogenation of Organic Molecules to Value-Added Chemicals Over a Ni–Fe Oxide Catalyst. *Adv. Energy Mater.* **2021**, *11*, 2101858. https://doi.org/10.1002/AENM.202101858.
61. Cui, X.; Xiao, P.; Wang, J.; Zhou, M.; Guo, W.; Yang, Y.; He, Y.; Wang, Z.; Yang, Y.; Zhang, Y.; et al. Highly Branched Metal Alloy Networks with Superior Activities for the Methanol Oxidation Reaction. *Angew. Chem.- Int. Ed.* **2017**, *56*, 4488–4493. https://doi.org/10.1002/anie.201701149.

62. Li, J.; Tian, X.; Wang, X.; Zhang, T.; Spadaro, M.C.; Arbiol, J.; Li, L.; Zuo, Y.; Cabot, A. Electrochemical Conversion of Alcohols into Acidic Commodities on Nickel Sulfide Nanoparticles. *Inorg. Chem.* **2022**, *61*, 13433–13441. https://doi.org/10.1021/acs.inorgchem.2c01695.
63. Candelaria, S.L.; Bedford, N.M.; Woehl, T.J.; Rentz, N.S.; Showalter, A.R.; Pylypenko, S.; Bunker, B.A.; Lee, S.; Reinhart, B.; Ren, Y.; et al. Multi-Component Fe-Ni Hydroxide Nanocatalyst for Oxygen Evolution and Methanol Oxidation Reactions under Alkaline Conditions. *ACS Catal.* **2017**, *7*, 365–379. https://doi.org/10.1021/acscatal.6b02552.
64. Zhao, B.; Xu, C.; Shakouri, M.; Feng, R.; Zhang, Y.; Liu, J.; Wang, L.; Zhang, J.; Luo, J.-L. L.; Fu, X.-Z. Z. Anode-Cathode Interchangeable Strategy for in Situ Reviving Electrocatalysts' Critical Active Sites for Highly Stable Methanol Upgrading and Hydrogen Evolution Reactions. *Appl. Catal. B Environ.* **2022**, *305*, 121082. https://doi.org/10.1016/j.apcatb.2022.121082.
65. Li, J. Nickel-Organic Frameworks as Highly Efficient Catalyst for Electrochemical Conversion of CH_3OH into Formic Acid. *Electrochem. commun.* **2023**, *146*, 107416. https://doi.org/10.1016/j.elecom.2022.107416.
66. Arshad, F.; ul Haq, T.; Khan, A.; Haik, Y.; Hussain, I.; Sher, F. Multifunctional Porous NiCo Bimetallic Foams toward Water Splitting and Methanol Oxidation-Assisted Hydrogen Production. *Energy Convers. Manag.* **2022**, *254*, 115262. https://doi.org/10.1016/j.enconman.2022.115262.